

Suwa data are from various sources (3) [T. Kobayashi (National Research Institute of Fisheries Science, Kanagawa, Japan), personal communication in 1996].

6. For rivers and large lakes, the freeze and breakup dates are at the location of observation and not necessarily for the river drainage system or lake as a whole. Several definitions of freezing and breakup are used for rivers. The transition between ice on and ice off is usually rapid, at least in the smaller lakes. The measurement error should be relatively small when compared to the observed rates of change. In the few winters when a water body did not freeze over, we set the freeze date to the latest observed freeze date for that water body and the breakup date to the earliest observed breakup date for that water body. All time series have been corrected for calendar changes.
7. These series do not all cover the entire 150 years because missing data occur in many of them. We analyzed linear trends to facilitate synthesis. However, some of the changes also can be interpreted as abrupt steps. In Lake Mendota, rather abrupt changes were detected in the late 1800s at the end of the Little Ice Age (8, 14, 16) and again in the 1970s with the interdecadal shift in the strength of the Aleutian low (7, 35). Toronto Harbor was not included in any estimates of average rates of change nor in statistical tests, except for sign tests concerning the consistency in direction of change; the slope for its breakup was extreme (3.3 standard deviations from the mean slope). This urban harbor may have been influenced by local factors.
8. R. A. Assel and D. M. Robertson, *Limnol. Oceanogr.* **40**, 165 (1995).
9. M. A. Palecki and R. G. Barry, *J. Clim. Appl. Meteorol.* **25**, 893 (1986).
10. M. Tanaka and M. M. Yoshino, *Weather* **37**, 252 (1982).
11. W. F. Rannie, *Clim. Change* **5**, 283 (1983).
12. F. Tramoni, R. G. Barry, J. Key, *Z. Gletscherkd. Glaziol.* **21**, 43 (1985).
13. I. I. Soldatova, *Russ. Meteorol. Hydrol.* **9**, 70 (1993).
14. D. M. Robertson, thesis, University of Wisconsin-Madison (1989).
15. S. Beltaos and T. D. Prowse, in *Contributions to IHP-V by Canadian Experts, UNESCO-International Hydrological Programme, IHP-V Technical Documents in Hydrology, No. 33* (United Nations Educational, Scientific and Cultural Organization, Paris, 2000), pp. 22–46.
16. D. M. Robertson, R. A. Ragotzkie, J. J. Magnuson, *Clim. Change* **21**, 407 (1992).
17. R. H. Wynne, J. J. Magnuson, M. K. Clayton, T. M. Lillesand, D. C. Rodman, *Limnol. Oceanogr.* **41**, 832 (1996).
18. D. M. Livingstone, *Clim. Change* **37**, 407 (1997).
19. R. A. Assel and L. R. Herche, in *Ice in Surface Waters: Proceedings of the 14th International Symposium on Ice*, H. Shen, Ed. (Balkema, Rotterdam, Netherlands, 1998), pp. 147–151.
20. T. K. Kratz, B. P. Hayden, B. J. Benson, W. Y. B. Chang, *Verh. Int. Ver. Limnol.*, in press.
21. W. L. Anderson, D. M. Robertson, J. J. Magnuson, *Limnol. Oceanogr.* **41**, 815 (1996).
22. D. M. Gray and T. D. Prowse, in *Handbook of Hydrology*, D. Maidment, Ed. (McGraw-Hill, New York, 1993), pp. 7.1–7.54.
23. T. D. Prowse and M. N. Demuth, *Nord. Hydrol.* **24**, 169 (1993).
24. L. C. Smith, *Phys. Geogr.* **21**, 46 (2000).
25. S. J. Vavrus, R. H. Wynne, J. A. Foley, *Limnol. Oceanogr.* **41**, 822 (1996).
26. H. Arakawa, *Cigaku Zashi* **63**, 193 (1954).
27. H. Simojoki, *Ann. Acad. Sci. Fenn.* **A52**, 1 (1940).
28. J. J. Magnuson et al., in *Freshwater Ecosystems and Climate Change in North America, A Regional Assessment*, C. E. Cushing, Ed. (Wiley, New York, 1997), pp. 7–53.
29. R. H. Wynne, T. M. Lillesand, M. K. Clayton, J. J. Magnuson, *Photogramm. Eng. Remote Sens.* **64**, 607 (1998).
30. J. T. Houghton et al., Eds., *Climate Change 1995, The Science of Climate Change: Contribution of Working Group I to the Second Assessment of the Intergovernmental Panel on Climate Change* (Cambridge Univ. Press, Cambridge, 1996).

31. J. F. B. Mitchell, T. C. Johns, J. M. Gregory, S. F. B. Tett, *Nature* **376**, 501 (1995).
32. E. Kuusisto, in *Snow Watch 92—Detection Strategies for Snow and Ice*, R. G. Barry, B. E. Goodison, E. F. Ledrew, Eds. (World Data Center, Asheville, NC, 1993), pp. 57–65.
33. A. Timmermann et al., *Nature* **398**, 694 (1999).
34. R. H. Wynne, *Verh. Int. Ver. Limnol.*, in press.
35. B. J. Benson, J. J. Magnuson, R. L. Jacob, S. L. Fuenger, *Verh. Int. Ver. Limnol.*, in press.
36. D.M.R. produced the graphics, B.J.B. developed and managed the database, J.J.M. and R.H.W. organized

the workshops, and all authors contributed data and improved the analyses, interpretations, and quality of the manuscript. We thank J. W. Mingle for assistance with manuscript preparation, those who contributed lake ice phenology data to the Lake Ice Analysis Group, the U.S. NSF's Division of Environmental Biology for supporting the research through grants DEB9632853 and DEB9416810, and W. Geller (Magdeburg, Germany) for calling attention to the Lake Constance data.

24 April 2000; accepted 29 June 2000

Northridge Earthquake Damage Caused by Geologic Focusing of Seismic Waves

Paul M. Davis,^{1*} Justin L. Rubinstein,¹ Kelly H. Liu,² Stephen S. Gao,² Leon Knopoff³

Despite being located 21 kilometers from the epicenter of the 1994 Northridge earthquake (magnitude 6.7), the city of Santa Monica experienced anomalously concentrated damage with Mercalli intensity IX, an intensity as large as that experienced in the vicinity of the epicenter. Seismic records from aftershocks suggest that the damage resulted from the focusing of seismic waves by several underground acoustic lenses at depths of about 3 kilometers, formed by the faults that bound the northwestern edge of the Los Angeles basin. The amplification was greatest for high-frequency waves and was less powerful at lower frequencies, which is consistent with focusing theory and finite-difference simulations.

The usual expectation is that damage to buildings from an earthquake in an urban area will be greatest near the epicenter and will decrease steadily with increasing distance. Traditionally, anomalous large damage has been attributed to site effects, such as amplified shaking of compliant soil structures (1, 2). For the Northridge earthquake (magnitude 6.7), soil effects in Santa Monica were found to be inadequate to explain the damage (3), because areas that had identical soils and were equidistant from the epicenter experienced less damage (Fig. 1).

The localized concentrations of high amplitudes of ground motion from the aftershocks of the Northridge earthquake suggested that focusing by deep geologic structures, which act like acoustic lenses, was likely to have caused the concentrated damage (Fig. 1) in Santa Monica during the main event (4).

Models have been proposed to test whether focusing can explain the aftershock amplitudes or the ground shaking from the main

event (5–11). These models have used published cross sections (12) of the geology beneath Santa Monica, and although they confirm that focusing may occur, they either give amplitudes that are too small (7) or the presumed site of the focus is located too far south (13). The need to model high frequencies at fine grid spacing (10 m) is so computationally intensive that such simulations have been restricted to two-dimensional (2D) structures and to unacceptably low frequencies (6, 11). Iterative inversion of the data is not yet feasible. However, the concentration of damage and the patterns of high aftershock amplification indicate that the proper treatment of the problem must take high frequencies into account, as well as the 3D subsurface structure. Our mapping of the underground geology is not sufficiently detailed to know, a priori, whether or not 3D focusing is important at any wavelength, much less at wavelengths on the order of 100 m. The geological cross sections are derived from logging of widely separated bore holes in the region (12, 13) and from extrapolation from the surface geology. We turned the problem around by attempting to identify focusing structures from an inversion of the aftershock data. To do this, we have developed a 3D forward model of deep basin focusing, albeit a simple one, that is suitable for iterative inversion.

¹Department of Earth and Space Sciences, University of California, Los Angeles, CA 90095–1567, USA. ²Department of Geology, Kansas State University, Manhattan, KS 66506–3201, USA. ³Institute of Geophysics and Planetary Physics and Department of Physics, University of California, Los Angeles, CA 90095–1567, USA.

*To whom correspondence should be addressed. E-mail: pdavis@ess.ucla.edu

REPORTS

The north-dipping Santa Monica fault and the basement of the Los Angeles basin form a convex low-velocity structure that is 3 to 4 km deep (12) and lies north of the fault trace. Depending on the velocity contrast between the bedrock and sediments and the radius of curvature of the structure, seismic waves passing through the structure apex should be concentrated at the surface. Under this proposal, incident waves refracted at the bedrock-to-basin interface would be converted into converging waves with a lens aperture (that is, a half-width) limited by the extent of the structure. As an idealization, we consider the cases of hemicylindrical and hemispherical lenses.

For wavelengths that are short as compared with the aperture dimension $2L$ and the focal length f of a hemicylindrical lens, the wave amplitude in the focal plane of a plane wave of initial amplitude A is

$$w(r) = \frac{2LA \sin \beta}{\sqrt{f\lambda} \beta} \quad (1a)$$

where

$$\beta = \frac{2\pi Lr}{f\lambda}$$

λ is the wavelength and r is the distance from the axis (14, 15). In this 2D case, the maximum amplification, which is at the center of the pattern, is

$$\frac{2L}{\sqrt{f\lambda}} \quad (1b)$$

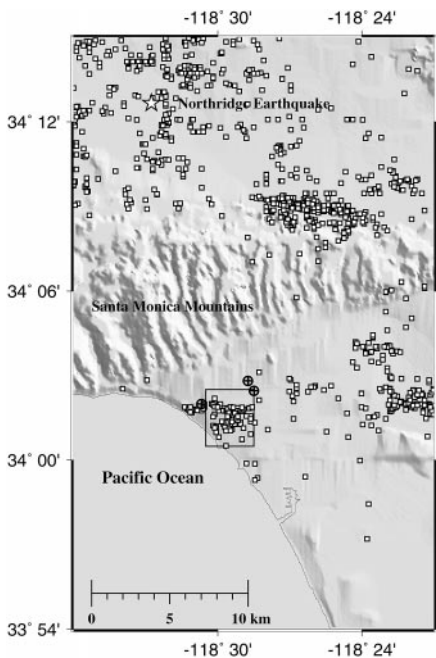


Fig. 1. Red-tagged (condemned) buildings (open squares) damaged by the 1994 Northridge earthquake (star). The crossed circles denote the locations of logged oil wells; the well closest to our region is the Occidental Marquez oil well lying just to the west.

In the case of a hemispherical lens, the amplitude in the focal plane is

$$w(r) = \frac{\pi L^2 A}{f\lambda} 2J_1(\beta)/\beta \quad (2a)$$

and the maximum amplification is

$$\frac{\pi L^2}{f\lambda} \quad (2b)$$

J_1 is the first-order Bessel function. The amplification in the 3D case is about the square of that in the 2D case, if the other parameters remain constant. Two-dimensional calculations therefore underestimate 3D focusing.

To determine the dependence of focusing in ranges where the wavelength is of the order of the diameter of the lens, we performed 2D finite-difference calculations for shear waves passing through focusing structures (Fig. 2). The source is taken to be the decaying sinusoid

$$f(t) = \cos(2\pi\nu t)e^{-(t/\tau_0)^2} \quad (3)$$

where ν is the frequency, t is time, and the decay constant τ_0 is several times the period $1/\nu$.

The elliptical interface between bedrock and basin sediments

$$x = \sqrt{2fy(1-\eta) - y^2(1-\eta^2)} \quad (4)$$

$$-L < x < L$$

$y = \text{constant}$ and $|x| > L$, concave toward the sediments, is perfectly focusing at a distance f from the vertex for normally incident plane waves from the bedrock; the axis of symmetry is the y axis. The constant is given by the

solution of Eq. 4 for $x = L$, and $\eta = v_2/v_1 < 1$ is the refractive index, where v_1 is the velocity in the bedrock and v_2 is that in the sediments. The radius of curvature at the vertex is $f(1-\eta)$. Snapshots of the wave field at various times (Fig. 2) show the development of focusing with high amplitudes, up to six times higher than that incident, at a distance of about 3 km from the lens. For the same parametric values as in Fig. 2, numerical values of amplification agree with the asymptotic values of Eq. 1 (Table 1) and show that the theory of Eq. 1 extends to frequencies as low as 3 Hz.

From Eqs. 1 and 2, the amplification increases with frequency. Eventually, high-frequency scattering of the seismic waves will limit the highest amplitudes attainable, when the sizes of the scatterers become comparable to the wavelengths of the incident radiation. Given the agreement in Table 1 in the 2D case, we expect that, for similar parameters, the amplifications will be represented well by Eq. 2b in the 3D case.

To test our proposal that geological focusing of seismic waves occurs beneath Santa Monica, we inverted the aftershock data using the maximum S -wave amplitudes (4) and the relative strengths of the spectra of S waves over the frequency bands from 1 to 4, 2 to 8, and 5 to 15 Hz. Individual S -wave spectra were calculated from 1 s of data centered on the peak arrival of the S wave. Geometric averages were taken of the individual spectra within each band. We divided individual values by coda wave values calculated as described by Gao *et al.* (4) in order to minimize site effects. Coda waves are thought to be omnidirectionally incident to a

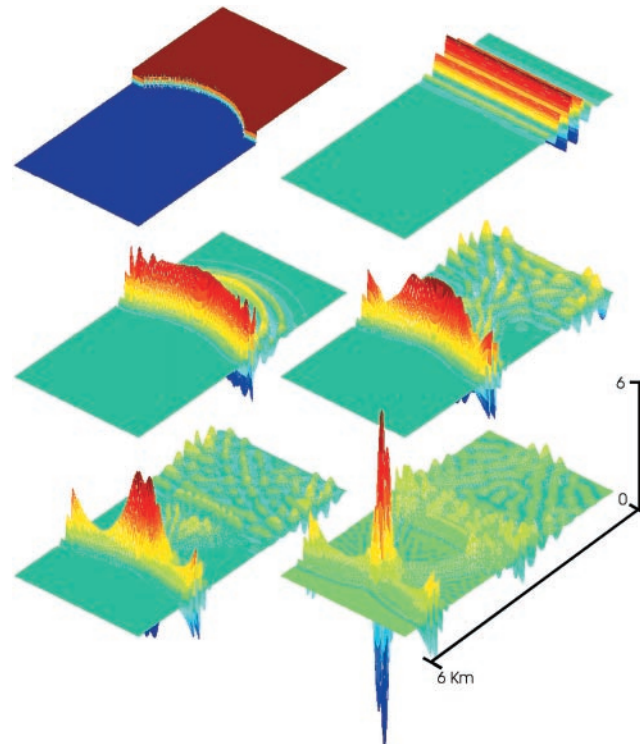


Fig. 2. Finite difference simulations of focusing from a 2D curved interface (top left). Snapshots are shown of a sinusoidal pulse of unit initial amplitude for $v_1 = 3.2$ km/s, $v_2 = 1.6$ km/s, $f = 3$ km, $L = 1.2$ km, and $\nu = 10$ Hz. The energy converges to generate a focused pulse of amplitude 6.0 relative to an amplitude of 1.8 immediately after passing through the interface (causing an amplification of 3.3). The region is 6 km long and 3 km wide. A grid spacing of 10 m was used.

REPORTS

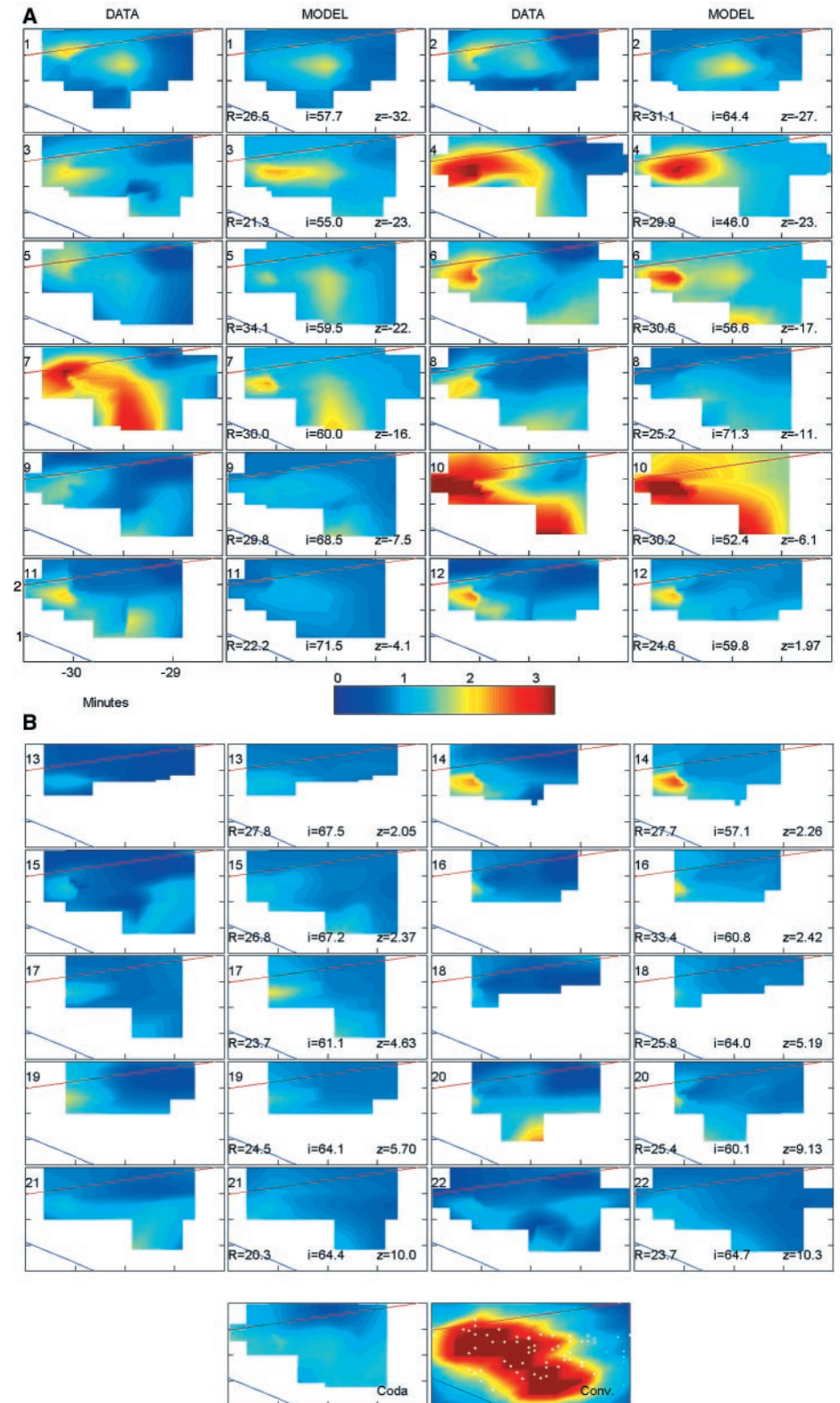
station. They are thus less dependent on focusing effects from deep structure, and we take their amplitudes as average estimates of near-surface site effects (16). Spectral and amplitude ratios were then formed by dividing by the corresponding average for all stations on bedrock north of the Santa Monica

fault. We analyzed data from 22 aftershocks. Each event was recorded at an average of 18 stations, thus providing 393 maximum amplitudes or 3×393 spectral ratio values.

Images of the distribution of spectral ratios for the 5- to 15-Hz band form three or more bright spots just south of the Santa Monica

fault. Their centers shift with the azimuth of the arriving waves (Fig. 3). We identified the bright spots as regions of focusing. The focusing pattern moves westward as the azimuths to the epicenters move eastward (Fig. 3) and exhibits a variable intensity that is maximum for azimuths to the west of north.

Fig. 3. Observed and modeled amplitudes of the 22 Northridge aftershocks used in this analysis. **(A)** Aftershocks 1 through 12; **(B)** aftershocks 13 through 22. The plots are derived from a spline fit to an average of 18 spectral ratios and are arranged so that arrivals from the northwest are plotted first, and arrivals to the east of north are plotted last. Those on the left side are measured amplitudes corrected for site effects, whereas those on the right give the theoretical images. R is the radial distance in kilometers to each aftershock, i is the angle of incidence at the interface, and z is the azimuth measured clockwise from north. The panel labeled "Coda" is an image of the coda, a measure of site effects. The lower right panel labeled "Conv" is the convolved effect of waves from the Northridge earthquake after passing through our model. The white dots correspond to condemned buildings. The buried trace of the inactive Santa Monica fault is depicted by the red line. The blue line corresponds to the coastline. Latitude and longitude coordinates are in minutes of arc from 34°N , 118°W .



REPORTS

We assumed that the basement-to-sediment contact geometry to the north of Santa Monica acts like an elongated lenslike structure. Due to irregularities in its geometry, it generates diffracted converging spherical waves at three locations on the surface (Fig. 3), each with amplitudes described by Eq. 2. Thus the overall structure contains three constituent lenses embedded in it. Although the focal planes of the converging spherical waves may not lie precisely on the surface, Eq. 2 is an adequate approximation provided they lie fairly close, because the amplitude pattern varies slowly on either side of the focal plane (14). We inverted the amplitude data to find the locations and apertures of three lenses that fit best the patterns in Fig. 3 in a least-squares sense (17). We approximated the elliptical shape of Eq. 4 as a spherical cap separating sediments and the bedrock; that is, a hemispherical lens of limited aperture. The apertures of the three caps were found to vary from 2×0.50 to 2×0.70 km, with centers at depths between 1.3 and 3.0 km. In each case, focal distance f was automatically set to be the distance along the central ray, with radii of curvature given by $f(1 - \eta)$. The emergence of the ray bundle from an aftershock was found by tracing the ray from its hypocenter through the bedrock and the sediments (Fig. 4) using a standard 1D model (18) of velocity variation. If the S -wave velocity is assumed to vary with increasing depth z in the bedrock as $v(z) = 3.0 + 0.06z$ km/s and in the sediments as $v(z) = 0.3 + 0.7z$ km/s, we reproduce the rays in the upper crust of the standard model. We found Eq. 2 to be an adequate representation of focusing for a lens with a velocity gradient, when the velocity contrast is taken to be the average velocity contrast across the interface. We used a Newton-Raphson iter-

ation to find the central ray for each aftershock that passes through each lens normal to its surface (Fig. 4). Let the location of the center of curvature of a lens be $[x_l, y_l, z_l]$ and the focal point be where the center of the ray bundle hits the surface $[x_f, y_f]$. The orientation of each spherical cap is assumed to be the same and to lie along the calculated direction of maximum amplification (4). For each cap, Eq. 2 is used to approximate the relative amplification at the i th site $[x_i, y_i]$ for the j th earthquake as

$$\text{amp}_{ij}(r) = A_0 + \sum_{\text{caps}} \frac{A_j(z, I) \pi L^2}{f \lambda} 2J_1(\beta_i) / \beta_i \quad (5)$$

where

$$\beta_i = \frac{2\pi L r_i}{f \lambda}$$

and

$$r_i^2 = (x_i - x_j)^2 + (y_i - y_j)^2.$$

$$A_j(z, I) = p_0 + p_1 \theta_j + p_2 \theta_j^2 + p_3 \theta_j^3$$

where

$$\theta_j = \sqrt{(z_j - z_0)^2 + (I_j - I_0)^2}$$

where $z_0 =$ azimuth and $I_0 =$ incidence angle of greatest amplification; that is, the critical direction (4).

The 19 unknowns in the inversion of the 393 data points are (z_0, I_0) , four coefficients p_i of the amplification polynomial, the three lens apertures L_p , the nine parameters describing the location of each lens, $[x_l, y_l, z_l]$, and A_0 , an offset term corresponding to the amplitude at infinity. The fit of the spectral ratio data (Table 2) (19) has reduced the power in the data by 90%.

Because of the paucity of stations near the focal points of the second and third

Table 1. Comparison between maximum amplifications from numerical simulation and theory.

Frequency	Wavelength	Numerical gain	Eq. 1b
10 Hz	160 m	3.2	3.4
5 Hz	320 m	2.6	2.4
3 Hz	500 m	2.1	1.9

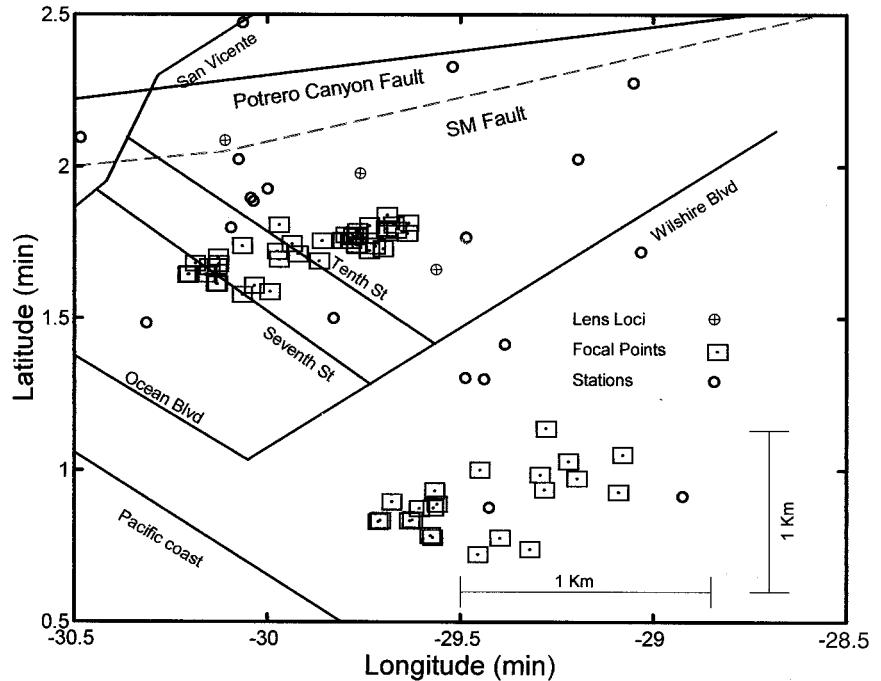
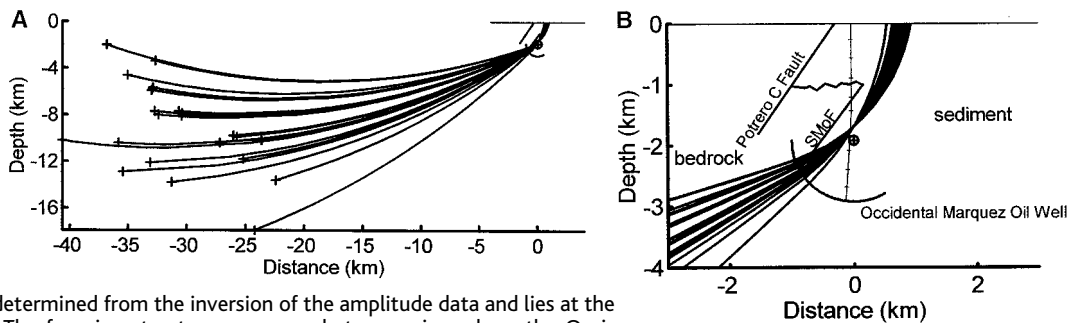


Fig. 5. Map showing the locations (crossed circles) of the three lenses that explain focusing patterns in Santa Monica aftershock amplitudes. The squares give the locations of focal points where the axial rays reach the surface. The open circles show the locations of the aftershock seismographic array.

Fig. 4. (A) Axial rays from 22 Northridge earthquake aftershocks through lens 1 to Santa Monica, projected onto a vertical plane running from north to south. The locations of the Potrero Canyon and Santa Monica faults are taken from Wright (12). It has been assumed that the focusing part of the basement-to-sediment interface is a spherical cap. (B) Expanded version of the model. The location of the cap is determined from the inversion of the amplitude data and lies at the sediment-to-basement interface. The focusing structure corresponds to a region where the Occidental Marquez oil well taps a reservoir estimated to contain 60 million barrels of oil. SMoF, Santa Monica fault.



REPORTS

Table 2. Lens locations and apertures. Errors derived from inversion of the data are one standard deviation.

Lens	Depth (km)	Latitude	Longitude	Half-aperture (km)
1	1.9 ± 0.1	34° 2.08' ± 0.05'	-118°30.11' ± 0.05'	0.70 ± 0.02
2	3.0 ± 0.5	34° 1.66' ± 0.09'	-118°29.56' ± 0.09'	0.50 ± 0.04
3	1.3 ± 0.1	34° 1.97' ± 0.05'	-118°29.76' ± 0.05'	0.60 ± 0.03

lenses (Fig. 5), their parameters are not well constrained. Their inclusion is significant at the 85% confidence level only, compared with over 99.99% for the first lens. Furthermore, their apertures overlap with the first lens; thus, the true situation is more complicated with a greater overall aperture. Comparison with the geologic cross sections given by (12) shows that the location and depth of the first lens (Table 2) are where the Santa Monica fault and the basin basement intersect to form a concave low-velocity structure at depth (Fig. 4).

We inverted the data from each of the spectral bands and maximum amplitudes. The variance reductions of the data were 77, 89, and 90% for the 1- to 4-Hz, 2- to 8-Hz, and 5- to 15-Hz bands, respectively, and were 86% for the maximum amplitudes. The decreased variance reduction at lower frequencies is consistent with the focusing being less efficient, as predicted by Eq. 2. The maximum amplitudes and the higher frequency spectral ratios give similar results for the geometry of the lenses, because the wave packets from which the peak amplitudes were picked predominantly have 10-Hz energy. Motions in the 10-Hz band of the spectrum are most likely to cause damage to single-story homes in Santa Monica.

We calculated the amplitude distribution for *S* waves passing through our three-lens structure from the Northridge earthquake (Fig. 3) and compared this distribution with the distribution of damaged buildings in Santa Monica. We adopted a subpatch model for the slip in the main shock (20) and treated each patch as an aftershock. We superimposed the signal from each subpatch (21). The resulting pattern of amplification has high values that correspond to the distribution of condemned buildings (Fig. 3) in the central and western regions.

We favor focusing from a deep (3-km) basin for the following reasons: The amplifications increase with frequency. The amplification pattern is concentrated over 0.5-km patches whose centers shift as the angles of incidence and azimuth shift. For a given wavelength of seismic radiation, the patch size determines the ratio of the aperture radius to focal length, L/f in Eq. 2, whereas the amplification determines L^2/f . The combination therefore determines L and f independently.

We estimate that site effects from compliant basin soil can explain an amplification by as much as a factor of 2, judged by late-arriving coda waves (Fig. 3) (4). Equations 1 and 2 show that 3D focusing effects can multiply this by an additional factor of 3 or more in localized regions. Our analysis is based on weak ground motion of *S* waves from aftershocks. The much greater amplitudes of the strong ground motion from the Northridge earthquake would have caused nonlinear behavior of the soil, which reduces amplitude. However the nonlinearity in Santa Monica (22) was not large enough to mask the localized amplification from focusing, but the actual value was probably smaller than that estimated here. We have assumed that the damage was caused by *S* body waves, which during the main event had the largest amplitudes in the strong ground motion record in Santa Monica. However, structural damage is related to the entire history of ground motion (23), including surface waves, basin edge effects (8), and other bursts of energy not in the *S*-wave window. This energy too may exhibit focusing on passing through the structures identified here, depending on frequency content and incidence angle. The one- and two-story buildings that were damaged during the Northridge earthquake had resonant frequencies in the range of 5 to 15 Hz (10). Our analysis shows that these frequencies would have been selectively focused more than lower frequency waves such as those of surface waves (8) or lower frequency body waves. The amplitudes at the critical direction (z_0, I_0) are found to have three times the values at angles 20° away from it. Thus, waves from other earthquakes will not focus as much as those from the Northridge event if the rays pass through the lens structures at different angles. If their epicenters are farther away, the frequencies of the most energetic spectral components will be lower, because of attenuation, and hence the bright spots will be less focused. For example, Santa Monica did not suffer anomalous damage at the time of the San Fernando (1971) earthquake.

References and Notes

1. A. C. Lawson, Ed., *The California Earthquake of April 18, 1906, Report of the State Earthquake Investigation Commission* (Carnegie Institute of Washington, Washington, DC, 1908), vol. I, part I, p. 253.

2. D. M. Boore and W. B. Joyner, *Bull. Seismol. Soc. Am.* **87**, 327 (1997).
3. G. A. Marshall and R. S. Stein, *USGS Open-File Rep.* **94-442** (1994).
4. S. Gao, H. Liu, P. M. Davis, L. Knopoff, *Bull. Seismol. Soc. Am.* **86**, S209 (1996).
5. H. Liu, thesis, University of California, Los Angeles (1998).
6. C. M. Alex and K. B. Olsen, *Geophys. Res. Lett.* **25**, 3441 (1998).
7. The authors in (6) suggest that focusing could explain only an amplification of 150% and that a combination of focusing and shallow basin effects may have been responsible for both the aftershock amplifications and the damage.
8. R. W. Graves, A. Pitarka, P. Somerville, *Bull. Seismol. Soc. Am.* **88**, 1224 (1998).
9. The authors in (8) suggest that shallow (less than 1 km) basin-edge effects may have been responsible for the Santa Monica damage, whereby constructive interference between basin and edge generated surface waves, and direct body waves caused localized amplification along the basin edge.
10. S. E. Hartzell, E. Cranswick, A. Frankel, D. Carver, M. Meremonte, *Bull. Seismol. Soc. Am.* **87**, 1377 (1997).
11. Graves *et al.* (8) compared their results with 1- to 6-Hz spectral ratios calculated by Hartzell *et al.* (10).
12. T. L. Wright, *Active Margin Basins: American Association of Petroleum Geologists*, Memoir 52, K. T. Biddle, Ed. (Tulsa, OK, 1991), p. 35.
13. Graves *et al.* (8) used the location of a fault scarp mapped by T. L. Pratt *et al.* [*Geophysics* **63**, 2479 (1998)] to define the location of the Potrero Canyon fault. Using this to locate the cross sections published by Wright, they fixed the northern edge of the Los Angeles basin, as defined by the buried trace of the Santa Monica fault, at about 0.75 km south of the map in Wright (12); hence their focusing structures are more southerly than ours. Our analysis of well-log data indicates that the Wright (12) location is to be preferred.
14. M. Born and E. Wolf, *Principles of Optics*, (Pergamon, New York, 1980).
15. D. Marcuse, *Light Transmission Optics* (Van Nostrand Reinhold, New York, ed. 2, 1982).
16. K. Aki, *J. Geophys. Res.* **74**, 615 (1969).
17. P. R. Bevington and D. K. Robinson, *Data Reduction and Error Analysis for the Physical Sciences* (McGraw-Hill, New York, ed. 2, 1997).
18. The Southern California Earthquake Center (SCEC) velocity model was used to obtain *S*-wave velocity variation in the sediments and bedrock beneath Santa Monica.
19. Other parameters of the inversion are: $A_0 = 1.15$; $Z_0 = -10.49$; $I_0 = 46.50$; $[P_0 \dots P_3] = [2.81, -0.2670, 0.0117, -0.0002]$.
20. Y. Zeng and R. Anderson, *Bull. Seismol. Soc. Am.* **86**, S71 (1996).
21. This model divides the source of the Northridge earthquake into a series of subevents on circular patches. Although it may overestimate high frequencies from the interior of the fault, it is satisfactory to model the spatial distribution of amplification of waves from the main event through our model.
22. S. C. Harmsen, *Bull. Seismol. Soc. Am.* **87**, 866 (1997).
23. M. D. Trifunac and A. G. Brady, *Bull. Seismol. Soc. Am.* **65**, 581 (1975).
24. We thank R. Graves for review and discussion; K. Olsen, T. Wright, T. Rockwell, and J. Dolan for helpful comments; and Y. Zeng for providing the Northridge earthquake sub-patch model. Supported by the Southern California Earthquake Center through NSF Cooperative Agreement EAR-8920136 and U.S. Geological Survey (USGS) Cooperative Agreements 14-08-0001-A0899 and 1434-HQ-97AG01718. The SCEC contribution number for this report is 528. Support from NSF grant EAR9416213 and USGS NEHRP contract 1434-HQ-97-GR-03115 is gratefully acknowledged.

22 May 2000; accepted 12 July 2000